1 **Additive Manufacturing of Biomechanically Tailored Meshes for Compliant Wearable and**

2 **Implantable Devices**

3

4 *Sebastian W. Pattinson,* * *Meghan E. Huber, Sanha Kim, Jongwoo Lee, Sarah Grunsfeld, Ricardo*

5 *Roberts, Gregory Dreifus, Christoph Meier, Lei Liu, Neville Hogan, A. John Hart**

6

7 Dr. S. W. Pattinson, Dr. M. E. Huber, Dr. S. Kim, Mr. J. Lee, Ms. S. Grunsfeld, Dr. R. Roberts,

8 Mr. G. Dreifus, Dr. C. Meier, Dr. L Liu, Prof. N. Hogan, Prof. A. J. Hart

9 Department of Mechanical Engineering, Massachusetts Institute of Technology, Cambridge, MA,

10 United States.

11 Dr. S. W. Pattinson

12 Department of Engineering, University of Cambridge, Cambridge, United Kingdom.

13 Dr. S. Kim

14 Department of Mechanical Engineering, Korea Advanced Institute of Science and Technology,

15 Daejeon, South Korea.

16 Ms. S. Grunsfeld

17 Department of Materials Science and Engineering, Massachusetts Institute of Technology,

18 Cambridge, MA, United States.

19 Dr. R. Roberts

20 School of Engineering and Sciences, Tecnologico de Monterrey, Mexico

21 Prof. N. Hogan

Department of Brain and Cognitive Sciences, Massachusetts Institute of Technology, Cambridge, MA, United States.

Email: swp29@cam.ac.uk , ajhart@mit.edu

Additive manufacturing (AM) of medical devices such as orthopedic implants and hearing aids is highly attractive because of AM's potential to match the complex form and mechanics of individual human bodies. Externally worn and implantable tissue-support devices, such as ankle or knee braces, and hernia repair mesh, offer a new opportunity for AM to mimic tissue-like mechanics and improve both patient outcomes and comfort. Here, it is demonstrated how explicit programming of the toolpath in an extrusion AM process can enable new, flexible mesh materials having digitally tailored mechanical properties and geometry. Meshes are fabricated by extrusion of thermoplastics, optionally with continuous fiber reinforcement, using a continuous toolpath that tailors the elasticity of unit cells of the mesh via incorporation of slack and modulation of filament-filament bonding. It is shown how the tensile mesh mechanics can be engineered to match the nonlinear response of muscle, incorporate printed mesh into an ankle brace with directionally specific inversion stiffness, and present further concepts for tailoring their 3D geometry for medical applications.

1. Introduction

Additive manufacturing (AM) enables the digitally-driven production of objects that are both individually customized and geometrically complex.[1] Considering the diversity and complexity of human bodies, AM is therefore well-suited to production of wearable and implantable devices

45 that offer enhanced performance or fit, including by customization, when compared to alternative

46 fabrication methods. These advantages have already led to numerous additively manufactured

47 medical devices, including orthopedic implants,[2] orthodontic aligners,[3] bone scaffolds,[4] and

48 prostheses.[5] However, importantly, all of these AM-enhanced devices interface with rigid parts

49 of the body, whereas soft tissues also often require mechanical support to prevent or heal injury.[6]

50   The mechanical characteristics of soft tissue support devices are critical to their

51 performance. For example, conventionally manufactured ankle braces, which restrict movement

52 to prevent (re-)injury can be bulky and poorly fitting. Implanted surgical mesh, which

53 mechanically supports tissue as it heals following surgery and is used in many of the estimated 20

54 million hernia surgeries around the world every year,[7] can restrict abdominal wall mobility and

55 lead to rigidity and discomfort.[8] These support devices could similarly benefit from the

56 customization and complex geometries enabled by AM.

57   Producing devices that replicate the mechanics of soft tissues is challenging, though,

58 because tissues such as muscle, tendons, and ligaments often have non-linear tensile stress-strain

59 responses, with an initially low stiffness that increases rapidly as the tissue becomes taut.[9] The

60 mechanical response of tissue is also highly anisotropic, varies significantly according to the

61 tissue type, and can be different for individual patients according to their body type and health

62 condition.[10] For instance, the tensile modulus of rat muscular tissue has been measured to be

63 approximately 0.1 MPa until a strain of 20%, and ~2.6MPa beyond 40% strain; for connective

64 tissue the relevant values are ~3 MPa to 10% strain and ~40MPa thereafter.[9] These tissues are

65 found in close proximity to one another, meaning that the overall mechanical properties have

66 spatially varying mechanics in addition to significant anisotropy. Additionally, soft tissue support

67 devices should be sufficiently porous to enable breathability (in the case of an external device) or

68 tissue integration (in the case of an implant).

69   Established methods to produce soft-tissue devices such as wearable braces and

70   implantable mesh typically use conventional fabrics made by knitting or weaving. While there

71   have been exciting innovations in conventional fabrics,[11],[12],[13] weaving is suited to regular

72   patterns and cannot adapt to sharp gradients in mechanical properties, while the looped topologies

73   used in knitting feature limited stiffness and control over 3D structure. Many researchers and

74   designers have explored the utility of AM to produce fabric-like geometries, such as thin,

75   continuous lattice structures or interlocked chainmail.[14],[15],[16],[17] Yet, adaptation of AM to

76   produce soft tissue supports requires detailed consideration of the local and global mechanics

77   necessary to provide meaningful utility, as well as design and toolpath planning algorithms

78   capable of adaptation to complex 3D topologies that match the contours of the body.

79   Here, we present a new, versatile approach to digital fabrication of biomechanically

80   tailored mesh materials using AM. The explicit programming of the toolpath of an extruded

81   thermoplastic, alongside optional reinforcement by continuous fiber, enables the additive

82   manufacturing of meshes with nonlinear elasticity to mimic the mechanics and conform to the 3D

83   structure of soft tissue. We demonstrate the advantages of this method by manufacturing and

84   testing an ankle brace that selectively prevents excessive inversion of the ankle, while leaving the

85   ankle otherwise free to move naturally in all other directions. We show the further possibilities

86   enabled by toolpath control in enhancing the conformity of the meshes to 3D structures by local

87   patterning of Negative Poisson's Ratio structures as well as using non-planar toolpaths to

88   modulate connectivity and to produce seamless 3-dimensional meshes.

89

90   **2. Results and Discussion**

91   To enable additive manufacturing of meshes with locally varying and anisotropic mechanics, we

92   introduce a hierarchical design where each mesh consists of an array of cells (**Figure 1**). By

93   specifying the mechanical properties of a cell, we specify the local and global mechanics of the

94   mesh. Each cell is composed of orthogonal elements, which determine the tensile response of

95   each cell in its respective direction, and can therefore establish anisotropic response.

96   Extrusion additive manufacturing, specifically using a thermoplastic elastomer (see

97   Methods) for demonstration herein, is chosen because of its simplicity and versatility. However,

98   unlike typical extrusion AM implementations where bulk objects are built with rigid bases for

99   attachment to the printer platform, here the mesh is directly printed as one or a few layers, with

100   explicit control of the toolpath to specify the desired mechanical properties of the mesh. A

101   continuous toolpath is important for mesh performance, because interruptions of the toolpath lead

102   to local defects that can compromise strength and therefore are especially undesirable for medical

103   applications. For meshes where each fiber running vertically or horizontally from one end of the

104   mesh to the other has uniform thickness, the toolpath follows a raster-pattern where all horizontal

105   lines are printed followed by the vertical lines. For meshes where a horizontal or vertical fiber

106   features locally varying thickness, which allows the mesh to exhibit a greater range of local

107   mechanical response, we use the graph theory-based toolpath planning algorithm developed by

108   Dreifus et al.[18] This algorithm is able to plot complex toolpaths where the extruder passes over

109   each part of the mesh a programmable number of times while minimizing discontinuities. Since

110   the extruder deposits a uniform thickness of thermoplastic each time it passes over a section of

111   the mesh, this allows for the local control of mesh thickness.

112

113   **2.1 Engineering tissue-like mesh mechanics**

114   To create printed mesh that accurately mimics the non-linear tensile response of soft tissue, we

115   must be able to control the stiffness at small strains (low) and at large strains (high), and the

116   transition strain at which the stiffness significantly increases (**Figure 2A,B**). For this, we take

117 inspiration from the wavy structure of collagen;[19] incorporating waves into each fiber segment

118 allows it to be stretched with an effective stiffness initially dominated by bending of the wave,

119 and then subsequently by stretching of the fiber once it is taut. Thus, for a single segment with

120 two waves and a total projected length l_e, the axial stiffness can be tuned by varying wave

121 amplitude (h_w) and width (l_w), relative to the total projected length which includes the straight

122 segments as well. As such, we model the nonlinear stretching behavior of the hyperelastic fiber

123 element as the superposition of the stretching of the straight and wavy segments. First, the axial

124 stiffness of the straight portion under applied force (F_e) is represented by a Mooney-Rivlin model

125 as[20]

126
$$\frac{F_e}{A_e C_1} = \left(1 + \frac{\mu_2}{\mu_1}\frac{1}{\lambda_{e,s}}\right)\left(\lambda_{e,s} - \frac{1}{\lambda_{e,s}^2}\right)$$
(Equation 1)

127 where μ_1 and μ_2 are material constants, A_e is the original cross-sectional area of the printed fiber,

128 and $\lambda_{e,s}$ is the element extension. The extension displacement due to stretching is therefore given

129 as

130
$$\delta_{e,s} = l_e\left(\lambda_{e,s} - 1\right)$$
(Equation 2)

131 On the other hand, the extension displacement due to bending (i.e., straightening) of the wavy

132 segment, is

133
$$\delta_{e,b} = 4\times\left\{h_w^2 + \left(\frac{l_w}{2}\right)^2\right\}^{1/2}\left[\cos\theta - \cos\left(\text{atan}\frac{2h_w}{l_w}\right)\right]$$
(Equation 3)

134 where θ is wave angle under tensile force of F_e, determined by the equilibrium of moments as

135
$$dF_e\left\{h_w^2 + \left(\frac{l_w}{2}\right)^2\right\}^{1/2}\sin\theta \cong -K'd\theta$$
(Equation 4)

136 Here, we assume the bending stiffness of the wave is constant and given as K'. The total

137 extension displacement δ_e is the summation of $\delta_{e,s}$ and $\delta_{e,b}$. (A detailed derivation of above

138 equations are described in Supporting Information). Thus, compared to tensile loading of a

139 straight segment only (**Figure 2B**), the wavy element exhibits a transition between low stiffness

140 (dominated by "opening" of the waves) at small strain, to higher stiffness at large strain

141 (dominated by stretching). The transition between bending- and stretching-dominated response is

142 also coincident with a maximum stiffness (**Figure 2C**). In **Figure 2E,F**, the estimated force-

143 strain and stiffness-strain curves of the two-wave element are compared to measurements on

144 printed samples. By changing the wave amplitude with all other parameters unchanged, we tailor

145 the strain (in terms of percent elongation relative to the original projected length) at which the

146 highest stiffness occurs, to above 40%.

147   To control the small strain stiffness we vary the extent of bonding between adjacent

148 elements, which is simply accomplished by printing adjacent elements in contact or with a small

149 lateral gap. Printing adjacent elements in contact causes the elements to become welded, thereby

150 effectively increasing their thickness perpendicular to the direction of strain.[21] The small strain

151 stiffness depends on the bending stiffness of the waves, and the bending stiffness increases in a

152 non-linear manner with the thickness of the fiber. As a demonstration, in **Figure 2G-H** we study

153 example units containing 5 parallel, wavy fiber elements; in one instance all 5 elements are

154 printed with lateral gaps; in another, the 3 central fibers are bonded; and, in the final instance, all

155 5 fibers are bonded. When all fibers are bonded the stiffness is relatively constant around

156 110N/m, while when all fibers are unbonded the stiffness is 20N/m until 10% strain, at which

157 point it rises to a maximum of 207N/m at 40% strain. The samples where 3 fibers are bonded

158 feature intermediate stiffness values of 53N/m at 10% strain rising to 150N/m at 40% strain.

159   Also, importantly the tensile behavior of the printed thermoplastic elastomer is resilient

160 under cyclic loading, and therefore the printed mesh elements can withstand repeated stretching

161 and release. For instance, we found no perceptible change in the tensile response of wavy

162 elements over 1800 cycles, to a peak strain of 32% (**Figure S1**). Furthermore, the fiber bending

163 stiffness, and therefore the low-strain stiffness, depends in a non-linear manner on fiber diameter.

164 Therefore, if the fiber becomes large enough, the bending stiffness will become similar to the

165 stretching stiffness, and the non-linear tensile behavior will no longer be observed.

166   This simple design allows the digital printing of mesh designs with mechanical behavior

167 that both qualitatively and quantitatively emulates the anisotropic, non-linear elasticity of natural

168 tissue. For instance, by tailoring the small strain and high strain stiffness, as well as the transition

169 strain, we show printed elastomer mesh matching the tensile response of rat muscle tissue, in both

170 orthogonal directions (**Figure 3A-B**).[22] In the direction perpendicular to the muscle fibril

171 orientation, the mesh exhibits a relatively constant modulus of 685kPa, while parallel to the

172 muscle fibrils the mesh features a modulus of 111kPa until a strain of 10%, and beyond 20%

173 strain the modulus increases to 453kPa. Here, we applied a strain rate of 0.05%/minute, which

174 was identical to that used by Takaza et al[22] for their tissue measurements.

175   Altogether, by the strategies described herein, printed unit cells can have tensile stiffness

176 values spanning 5 orders of magnitude (**Figure 3C**), from 20kN/m to 0.5N/m, and, by controlling

177 the geometry and connectivity of the fiber elements, the transition strain can be tuned as well.

178 The highest stiffness is achieved by incorporating continuous fiber such as stainless steel wire

179 into the mesh, as discussed in detail later.

180

181 **2.2 A mesh-reinforced brace to prevent ankle inversion**

182 As a demonstration of a potential application of the nonlinear, muscle-like mechanics of the

183 printed mesh, we built a prototype brace to selectively reinforce the inversion stiffness of the

184 human ankle while leaving it otherwise free to move naturally. Ankle inversion is one of the most

185 common injuries in humans and often leads to residual problems such as ankle instability and

186 pain, especially after recurring sprains.[23],[24],[25],[26] As a result, soft or semi-rigid ankle braces

187 (typically made of lycra/neoprene or nylon/polyester, respectively) are often used to prevent

188 recurrent injuries after a mild/moderate ankle sprain.[27] However, these devices typically

189 uncomfortably restrict most or all of the degrees of freedom of the ankle, which limits their use

190 by patients, can cause muscle to atrophy leading to increased susceptibility to future injury, and

191 also negatively affects sports performance.[28],[29]

192   Ankle braces that are anatomically customized, either directly to the patient or made in a

193 variety of shapes and sizes, and having locally defined, non-linear, mechanics, could both restrict

194 excessive motion in undesired directions (e.g., inversion) and ideally enable natural motion in

195 other directions. We thus prototyped a device to selectively stiffen the ankle when it undergoes

196 inversion (**Figure 4a**), including a strip of printed mesh placed on the outside of the ankle, such

197 that it will experience tension when the ankle attempts to invert. Importantly, the extensibility and

198 transition strain of the mesh were designed to allow a degree of inversion while stiffening

199 significantly once this is exceeded. A brace was fabricated by fastening the mesh to an assembly

200 of 3D printed components, enabling it to be fitted around a shoe and interfaced with the

201 instrumented measurement device. This setup ensured a rigid attachment to the body and that the

202 forces were transferred via the non-linear mesh. Finally, the wavy component of the mesh (which

203 has the non-linear tensile response) is layered without bonding, to make it flexible in bending out

204 of plane and therefore allowing it to buckle, so that it does not affect the stiffness in eversion.

205   We then measured the static component of multivariable ankle mechanical impedance, a

206 generalization of ankle stiffness, with and without the mesh placed over the ankle joint. Using an

207 Anklebot (Bionik Laboratories Corporation, Watertown, MA), the static torque-angle relation in

208 the inversion/eversion (IE) and dorsiflexion/plantarflexion (DP) directions were simultaneously

209 measured and used to estimate ankle stiffness in different directions within IE-DP space.[23]

210   Data from 4 subjects indicate that our brace is able to selectively increase the linear

211   approximation of effective ankle stiffness in inversion while leaving it relatively unaffected in

212   other directions (**Figure. 4C,D** and **Figure S4**). Across all 4 subjects, wearing the mesh increased

213   the effective ankle stiffness by an average of 78.69% in the inversion direction and only by

214   14.27% in eversion, -1.59% in dorsiflexion, and -1.40% in plantarflexion. Moreover, the results

215   show that the added stiffness is non-linear (**Figure 4D** and **Figure S4**). The torque required to

216   achieve angular displacement in inversion is relatively similar whether or not a brace is worn up

217   to ~1.5°, after which the stiffness of the ankle with the brace becomes steadily higher until it is

218   approximately ~50% greater than that of the bare ankle at an inversion of 15°. These results

219   suggest that meshes with non-linear tensile response are promising candidates for making future

220   braces that only prevent motion that will lead to injury, while otherwise leaving the ankle to move

221   freely. Such braces may have significant potential both as prophylactic braces as well as aiding

222   rehabilitation by enabling patients to resume activities more quickly.

223

224   **2.3 Printing fiber-reinforced mesh**

225   Thermoplastic elastomer meshes can achieve widely tailored mechanical properties for use in

226   devices such as the ankle brace described above. However, many potential applications of printed

227   mesh—including implantable hernia mesh—will demand greater stiffness and strength.

228   Specifically, the stiffness of a strained elastomer mesh depends on the cross-sectional area of its

229   fibers and therefore is proportional to the amount of printed material. However, to treat injury of

230   some connective tissues an even greater stiffness is needed in the large strain regime, preventing

231   excessive deformations and, ultimately, failure; for contrast, see **Figure S2a** where one all-

232   elastomer unit cell breaks at 2.4N.

233   A strategy to digitally fabricate stronger mesh is to incorporate synthetic fibers or threads

234   into the printing process. AM of fiber-reinforced components is well-known, particularly via

235   placing a thermoplastic-coated thread into the layers of 3D components such as mechanical

236   fixtures and brackets.[30] While this gives components with significantly enhanced flexural

237   rigidity and strength, for printing mesh it is desirable to leave the fiber unconstrained in the open

238   areas of each unit cell, to enable it to become taut only at a critical strain where the highest

239   stiffness is needed. In other words, a continuous fiber such as a fine metal wire is compliant in

240   bending like printed thermoplastic filament, but much more rigid in tension.

241   To incorporate continuous fiber into mesh, we implement a second (unheated) nozzle on

242   the extrusion 3D printer, and thread the fiber through the nozzle. This allows the deposition of

243   continuous fiber without a thermoplastic sheath by instead using an adhesive substrate to

244   passively pull fiber out of a nozzle (**Figure 5B-C** and Supporting Video). We place a film with

245   adhesive on both sides onto the printer bed, and then extrude a layer of thermoplastic onto this,

246   according to the thermoplastic mesh design but leaving gaps where continuous fiber is desired.

247   We move the fiber nozzle over the substrate, causing the fiber to follow the path of the nozzle and

248   stick to the adhesive. The continuous fiber is patterned such that it overlaps with the already

249   extruded thermoplastic in some regions. In order to bond the fiber to the rest of the mesh, we

250   deposit another layer of thermoplastic in an identical pattern to the first layer, which sandwiches

251   the fiber. Here, we print stainless steel thread as the continuous fiber, which is impervious to the

252   temperatures used for thermoplastic extrusion (~210°C). Many other fiber materials with suitable

253   thermal stability could be used, such as carbon fiber and Kevlar.

254   Here, a mesh that permits a continuous toolpath is important to minimize need to cut the

255   fiber. And, because the continuous fiber cannot change direction unless it is in contact with the

256   adhesive substrate, the fiber nozzle must be very close to the print bed for accurate patterning.

257   Also, the cell must have a minimum curvature due to the forces that build up in the fiber during

258   bending. Finally, there has to be overlap between continuous fiber and elastomeric matrix to

259   allow the continuous fiber to be bonded to the mesh. Taking these into consideration, we

260   designed the unit cell shown in **Figure 5D** for use with continuous fiber.

261   These unit cells exhibit greater large strain stiffness than is possible with the all-elastomer

262   designs, while retaining a large open area. In particular, the tensile response (**Figure 5E**) of these

263   unit cells is governed by the elastomer at small strains (180 N/m stiffness), and stiffens sharply

264   when the steel fiber becomes taut (7.3kN/m). As with the all-elastomer unit cells, the strain at

265   which this transition occurs can be controlled by the wave amplitude of the pre-made fiber, and

266   the large strain stiffness is governed by the fiber properties. The ultimate strength depends on the

267   mesh design and the continuity of fiber path, but can be limited by the fiber-polymer adhesive

268   strength.

269

270   **2.4 Towards conformal, customized mesh-based assistive devices**

271   Looking forward to broader uses of digitally tailored mesh in wearable and implantable devices,

272   another important capability is conformality to 3D surfaces, both for increased comfort as well as

273   to controllably transfer mechanical forces. This will ultimately be achieved by more

274   sophisticated planning algorithms that relate the desired shape and mechanics to the mesh

275   topology, and plan the printer toolpath accordingly including via non-planar printing layers.[31]

276   Toward this goal, we show three further capabilities: (1) controlling drape by modulating bonding

277   between orthogonal filaments; (2) coupling in-plane and out-of-plane displacements via mesh

278   cells with negative Poisson's ratio; and (3) printing mesh onto 3D templates.

279   Conventional textiles are highly conformable because the constituent fibers (both within

280   individual threads and yarn, and within knits and weaves) can slip over one another. It was

281 explained earlier that slip is undesirable for precise control of in-plane stress and strain; however,

282 it can be useful if placed locally to allow mesh conformality. In the printing process, we therefore

283 locally enable fiber slip by lifting the printer nozzle as it passes over filament in the mesh, such

284 that the newly printed filament cools before it contacts the underlying filament on the print bed

285 (**Figure 6a**). Printing fibers that are not bonded significantly enhances the drape of an exemplary

286 printed fabric. Comparing two otherwise identical specimens placed in a cantilever configuration,

287 the unbonded fabric deflects vertically ~230% more than the bonded fabric. Over a sphere (here,

288 a golf ball), the unbonded fabric wraps the sphere while the bonded one does not. Control of the

289 Poisson's ratio at the unit cell-level can also allow the fabric to conform to a curved surface

290 without folding.[32] As a demonstration, a printed mesh with locally negative Poisson's ratio is

291 placed onto the author's knee (**Figure 6b**).[33] When the same mesh is stretched in-plane by hand,

292 it can bulge upward (Supplementary Video), suggesting that inverse design of the mesh pattern

293 can enable complex strain profiles to be followed.

294 Last, explicit control of the printing toolpath also enables the production of non-planar meshes

295 (**Figure 6c**), providing another means for devices to conform to the body while maintaining the

296 desired mechanics for biomechanical reinforcement. To print mesh for a glove-like brace on a

297 hand, we first 3D print support structure designed to approximate the height and position of a

298 knuckle. Next, we cover these knuckle templates with tape to prevent the extruded mesh from

299 adhering to the support directly. A graph-theory based, algorithm developed in a separate study,

300 is used to plan the toolpath over the prescribed boundary and curved topography, with a

301 minimum number of discontinuities.[18] The mesh is then sewn to a glove, and is therefore

302 designed to counteract spasticity (increased stiffness) by providing extension forces to a clenched

303 fist, which can occur from neurological injuries such as acute ischemic stroke.[34]

304

305 **3. Conclusion**

306 We have demonstrated a route to digital tailoring of compliant mesh materials, which may find

307 wide application in the design and manufacturing of wearable and implantable devices.

308 Importantly, the printed mesh architecture enables engineered nonlinear mechanics that can

309 mimic those of soft tissue and enable 3D conformality to the body. We demonstrate a process

310 where explicit control of the printer toolpath, a hierarchical mesh design, and new hardware for

311 patterning of continuous fibers enables the additive manufacture of parts with locally controlled

312 mechanics matching those of individuals' soft tissue. Moreover, we demonstrate how our

313 toolpath software enables the production of meshes with 3D structure that allows better

314 conformability to the body through inter-fiber bonding control for improved drape, locally

315 patterned negative Poisson's Ratio regions, and 3D toolpaths printed onto support structures. We

316 produce an example ankle brace that shows the potential of controlled non-linear tensile response

317 by letting the ankle move freely unless it inverts to an excessive extent, as well as a glove with an

318 embedded mesh designed to conform to the hand. Inverse design of meshes, where mesh material

319 and geometry are designed to generate desired properties would enable unprecedented novel

320 devices that seamlessly interact with the body, and thereby improve the lives of countless patients

321 suffering from conditions ranging from ankle or other joint sprain to hernia and tremors.

322

323 **4. Experimental Section**

324 *Printing:* Extrusion is done using a commercial 3D printer Printrbot Simple Metal. Thermoplastic

325 Polyurethane (Ninjaflex) is the primary matrix material used, while stainless steel thread (0.4mm

326 thick 3 ply thread, 316L alloy, Adafruit Industries) is the pre-made continuous fiber. For

327 continuous fiber deposition, the substrate is made adhesive through the use of double-sided tape.

328   The nozzle used to guide the continuous fiber is a tapered nozzle from Nordson (product

329   number). We printed a holder for the nozzle to sit next to the extruder as shown in **Figure S1**.

330   *Toolpath planning:* The toolpath is essential to achieving the best mechanics/morphology from

331   the fabrics and therefore we wrote our own software in the Python language to do this. The

332   software takes as input the desired array of unit cells in the mesh alongside printing parameters

333   such as rate and temperature, and translates these into g-code, which are the instructions for the

334   printer. The g-code output by the Python software is then input into Repetier-Host software as

335   manual g-code, which passes the instructions to the printer.

336   *Mechanical Testing:* Tensile testing was conducted using an Instron 1125 machine with a 20000

337   lb. (2511-305) and a 100N load cell (Omega S-type). All tests were conducted taking 3000 data

338   points per minute at a displacement rate of 5 mm min^{-1}. Flexural testing was carried out by

339   attaching a mass to fibers or fabrics and measuring the vertical displacement.

340   *Finite Element Modeling:* For the modeling of individual fibers, a finite element formulation

341   based on the so-called geometrically exact Simo-Reissner beam theory, incorporating the

342   deformation modes of axial tension, shear, torsion and bending, has been applied. The

343   formulation is geometrically non-linear and accounts for arbitrarily large displacements and

344   rotations as well as for finite strains. The stress-strain relationship is based on an elastic

345   constitutive law defined by Young's modulus and Poisson's ratio. All simulations have been

346   conducted in a quasi-static manner employing the in-house finite element research code BACI

347   developed at the Institute for Computational Mechanics at the Technical University of Munich.

348   *Ankle measurements experimental setup:* Four subjects (age: 27±4 yrs; gender: 3 male, 1 female)

349   with no reported history of biomechanical or neuromuscular disorders participated in the

350   experiment. All gave informed written consent before the experiment. The experimental protocol

351   was reviewed and approved by the Institutional Review Board of the Massachusetts Institute of

352 Technology. Subjects wore a modified shoe and a knee brace on their right leg, to which the

353 Anklebot was attached.[35] The knee brace was attached to the chair such that weight of the robot

354 and leg were fully supported and the foot did not contact the ground (Figure 4a). Subjects were

355 instructed to remain relaxed during the experiment.

356   Each trial consisted of 24 movements (an inward and outward motion along 12 equally-

357 spaced directions in IE-DP space, with a nominal displacement amplitude of 15° in each direction

358 at constant speed of 5°/s) (Figure 4b). The robot speed was selected to maintain a quasi-static

359 relationship between measured torque and displacement and avoid evoking spindle-mediated

360 stretch reflexes. For each movement, the robot moved the ankle along a commanded trajectory

361 and recorded applied torque and actual angular displacement at 200 Hz sampling frequency.

362   Four trials were conducted in each of two conditions: *no mesh* and *mesh*. During trials in

363 the *mesh* condition, one end of the mesh was attached to the knee brace and the other was

364 attached to the shoe on the lateral side of shank, parallel to the tibia (Figure 4a).

365 *Ankle Measurement Data Analysis:* In each condition, a vector field, V, defined as

$$(\tau_{IE}, \tau_{DP}) = V(\theta_{IE}, \theta_{DP})$$

366 was approximated from measured multivariable torque–angle relation in IE-DP space for each

367 individual subject. θ_{IE} and θ_{DP} are the angular displacements in the IE and DP directions,

368 respectively, and τ_{IE} and τ_{DP} are the corresponding applied torques. Figure 4c shows 2D slices of

369 the two vector fields (*mesh* and *no mesh*) in the inversion direction for two example subjects. As

370 expected, the mesh added nonlinear stiffness to the ankle.

371   To evaluate the directional effect of the mesh, ankle stiffness was also evaluated for all

372 directions in each condition (*mesh* and *no mesh*). Ankle stiffness for a given direction was

373 calculated as the slope of a linear approximation of the vector field in that direction.

374

Supporting Information

Supporting Information is available from the Wiley Online Library or from the author.

Competing Interests

S.W.P. and A.J.H. are inventors on an MIT patent application: Systems, Devices, and Methods for Extrusion-Based Three-Dimensional Printing. U.S. Ser. No. 15/376,416. PCT Ser. No. PCT/US16/66205. This application primarily addresses the printing process for the mesh. S.W.P., A.J.H., M.E.H., J.L., and R.R. are also inventors on an MIT provisional patent application: Additively Manufactured Mesh Materials, Wearable and Implantable Devices, and Systems and Methods for Manufacturing the Same, U.S. Ser. No. 62/797,044. This application primarily addresses applications for the mesh.

Received: ((will be filled in by the editorial staff))
Revised: ((will be filled in by the editorial staff))
Published online: ((will be filled in by the editorial staff))

401   References

402   [1]   S. Patra, V. Young, *Cell Biochem. Biophys.* **2016**, *74*, 93.

403   [2]   S. L. Sing, J. An, W. Y. Yeong, F. E. Wiria, *J. Orthop. Res.* **2016**, *34*, 369.

404   [3]   M. Martorelli, S. Gerbino, M. Giudice, P. Ausiello, *Dent. Mater.* **2013**, *29*, e1.

405   [4]   R. Trombetta, J. A. Inzana, E. M. Schwarz, S. L. Kates, H. A. Awad, *Ann. Biomed. Eng.*
406   **2017**, *45*, 23.

407   [5]   Y. He, G. Xue, J. Fu, *Sci. Rep.* **2015**, *4*, 6937.

408   [6]   P. P. Pott, M. L. R. Schwarz, R. Gundling, K. Nowak, P. Hohenberger, E. D. Roessner,
409   *PLoS One* **2012**, *7*, 1.

410   [7]   A. Kingsnorth, K. LeBlanc, *Lancet* **2003**, *362*, 1561.

411   [8]   K. Junge, U. Klinge, A. Prescher, P. Giboni, M. Niewiera, V. Schumpelick, *Hernia* **2001**,
412   *5*, 113.

413   [9]   B. Calvo, A. Ramirez, A. Alonso, J. Grasa, F. Soteras, R. Osta, M. J. Munoz, *J. Biomech.*
414   **2010**, *43*, 318.

415   [10]   M. Śmietański, K. Bury, A. Tomaszewska, I. Lubowiecka, C. Szymczak, *Surg. Endosc.*
416   *Other Interv. Tech.* **2012**, *26*, 1461.

417   [11]   J. Mccann, J. Mankoff, J. Hodgins, **2011**, *35*, 1.

418   [12]   B. Bickel, B. Moritz, M. A. Otaduy, H. R. Lee, W. Matusik, **2009**.

419   [13]   M. Akbari, A. Tamayol, S. Bagherifard, L. Serex, P. Mostafalu, N. Faramarzi, M. H.
420   Mohammadi, A. Khademhosseini, *Adv. Healthc. Mater.* **2016**, n/a.

421   [14]   A. Johnson, G. A. Bingham, D. I. Wimpenny, *Rapid Prototyp. J.* **2013**, *19*, 199.

422   [15]   J. White, M. Foley, A. Rowley, *3D Print. Addit. Manuf.* **2015**, *2*, 145.

423   [16]   H. Peng, J. Mankoff, S. E. Hudson, J. Mccann, **2015**.

424   [17]   P. Bettini, G. Alitta, G. Sala, L. Di Landro, *J. Mater. Eng. Perform.* **2017**, *26*, 843.

425   [18]   G. Dreifus, K. Goodrick, S. Giles, M. Patel, R. M. Foster, C. Williams, J. Lindahl, B. Post,

426   A. Roschli, L. Love, V. Kunc, *3D Print. Addit. Manuf.* **2017**, *4*, 98.

427   [19]   T. Ushiki, *Arch. Histol. Cytol.* **2002**, *65*, 109.

428   [20]   A. Bower, *Applied Mechanics of Solids*; CRC Press, 2009.

429   [21]   J. E. Seppala, S. Hoon Han, K. E. Hillgartner, C. S. Davis, K. B. Migler, *Soft Matter* **2017**,

430   *13*, 6761.

431   [22]   M. Takaza, K. M. Moerman, J. Gindre, G. Lyons, C. K. Simms, *J. Mech. Behav. Biomed.*

432   *Mater.* **2012**, *17*, 209.

433   [23]   C. Doherty, E. Delahunt, B. Caulfield, J. Hertel, J. Ryan, C. Bleakley, *Sport. Med.* **2014**,

434   *44*, 123.

435   [24]   L. Tanen, C. L. Docherty, B. Van Der Pol, J. Simon, J. Schrader, *Foot Ankle Spec.* **2014**, *7*,

436   37.

437   [25]   and D. C. T. J. P. Gerber, G. N. Williams, C. R. Scoville, R. A. Arciero, *Foot Ankle Int.*

438   **1998**, *19*, 653.

439   [26]   M. S. Yeung, K. M. Chan, C. H. So, W. Y. Yuan, *Br. J. Sports Med.* **1994**, *28*, 112.

440   [27]   E. Eils, C. Demming, G. Kollmeier, L. Thorwesten, K. Völker, D. Rosenbaum, *Clin.*

441   *Biomech.* **2002**, *17*, 526.

442   [28]   L. Deberg, M. T. Andani, M. Hosseinipour, M. Elahinia, *Smart Mater. Res.* **2014**, 572094.

443   [29]   K. Tamura, K. N. Radzak, R. E. Vogelpohl, B. A. Wisthoff, Y. Oba, R. K. Hetzler, C. D.

444   Stickley, *Gait Posture* **2017**, *58*, 108.

445   [30]   R. Matsuzaki, M. Ueda, M. Namiki, T.-K. Jeong, H. Asahara, K. Horiguchi, T. Nakamura,

446   A. Todoroki, Y. Hirano, *Sci. Rep.* **2016**, *6*, 23058.

447   [31]   R. J. A. Allen, R. S. Trask, *Addit. Manuf.* **2015**, *8*, 78.

448   [32]   M. Konakovic, J. Panetta, K. Crane, M. Pauly, *ACM Trans. Graph.* **2018**, *37*, 1.

449   [33]   A. Clausen, F. Wang, J. S. Jensen, O. Sigmund, J. A. Lewis, *Adv. Mater.* **2015**, *27*, 5523.

450   [34]   P. P. Urban, T. Wolf, M. Uebele, J. J. Marx, T. Vogt, P. Stoeter, T. Bauermann, C.

451   Weibrich, G. D. Vucurevic, A. Schneider, J. Wissel, *Stroke* **2010**, *41*, 2016.

452   [35]   H. Lee, P. Ho, M. A. Rastgaar, H. I. Krebs, N. Hogan, *J. Biomech.* **2011**, *44*, 1901.

453

456
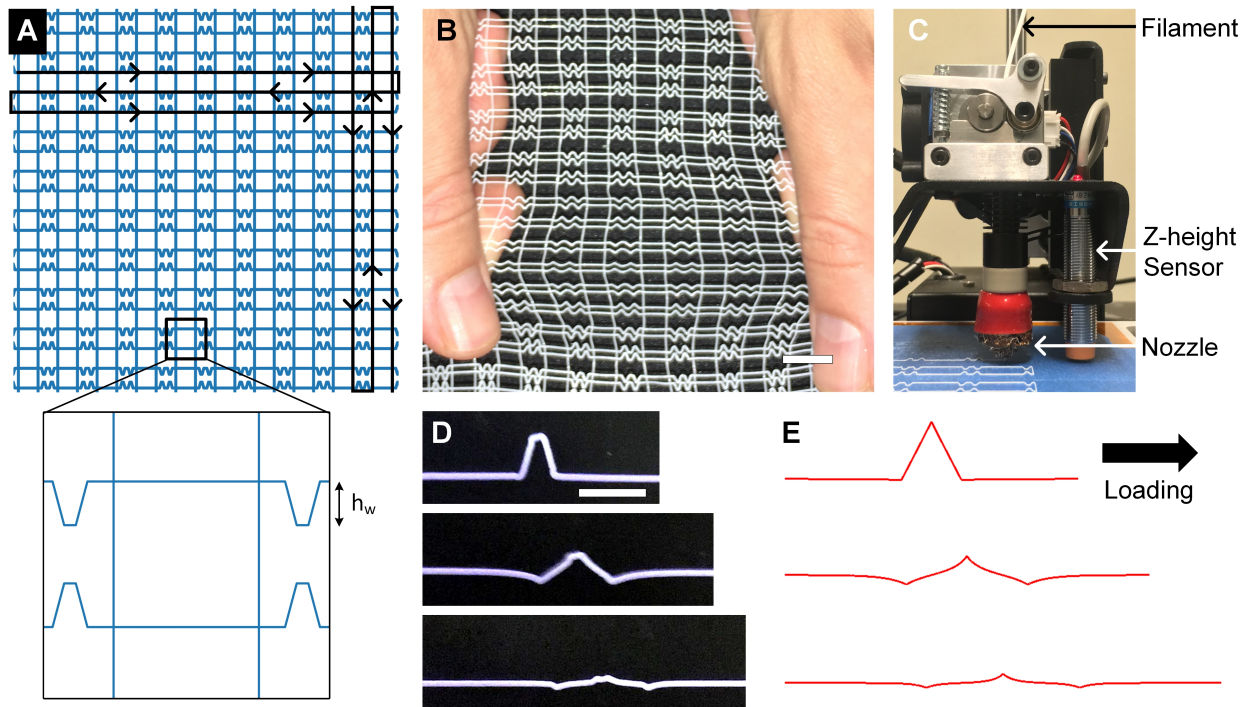
457   **Figure 1:** a) Schematic of hierarchical mesh fabrication approach with black lines indicating

458   toolpath; h_w indicates the wave height. b) Exemplary printed mesh (scale bar 10mm). c) Extruder

459   setup used for mesh printing. d) Image of printed fiber with a wave (scale bar 5mm), with

460   increasing tensile strain from top to bottom. e) Finite element simulations of an individual fiber

461   with a wave, with increasing tensile strain from top to bottom.

462
463
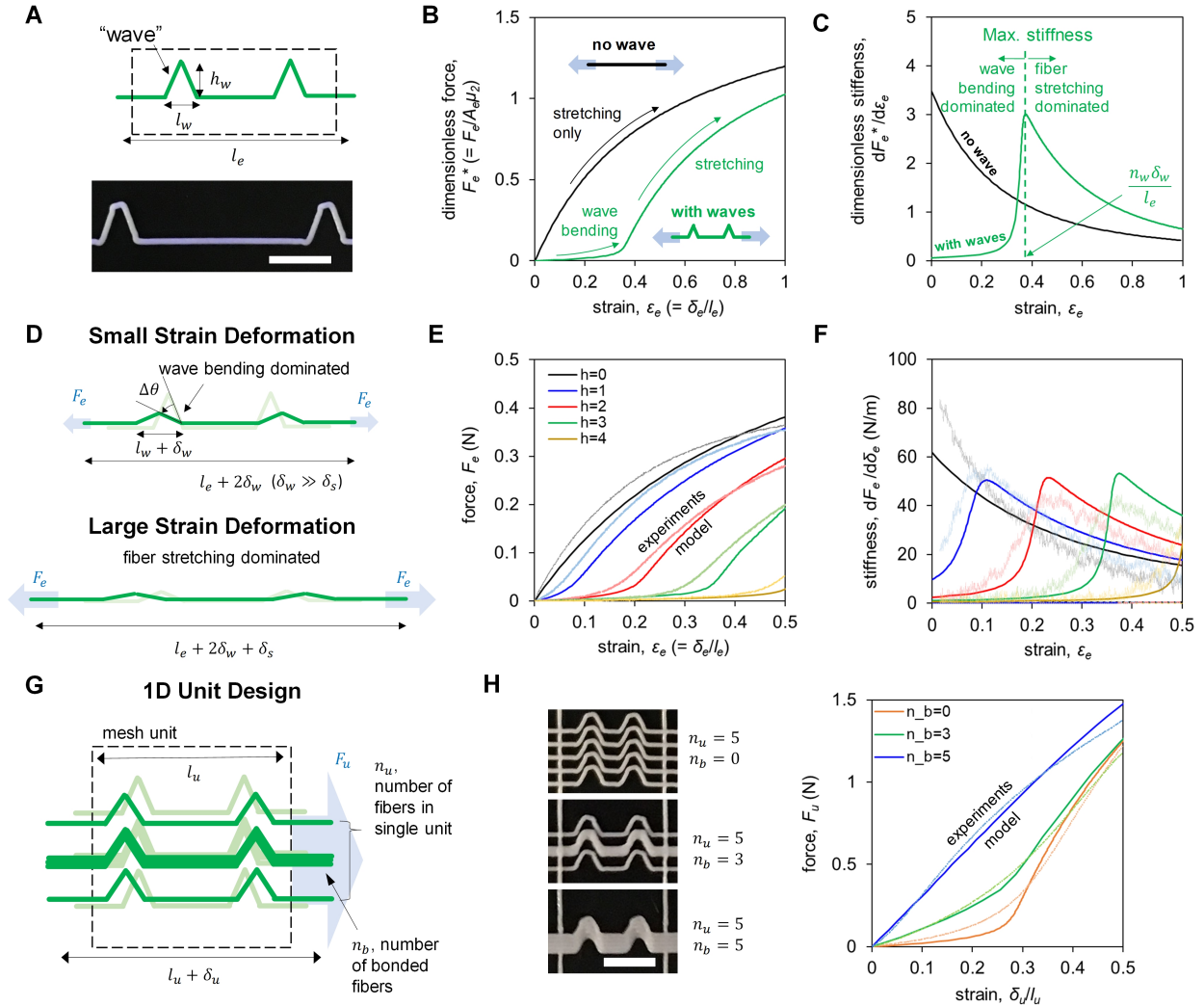
Figure 2: Methods of controlling the non-linear tensile response of individual fibers ("elements"). a) Schematic and image of fiber waves used to introduce non-linear behavior (scale bar is 5mm). b) Mechanical model of tensile response of a fiber with a wave. c) Stiffness of the model fiber in the previous figure d) Schematic describing the mechanical model. e) Controlling the low-to-high strain transition by varying the wave height. f) Stiffness of the fibers versus strain, for the same parameters as in the previous figure. g) Schematic showing variation in fiber bonding for low strain stiffness modulation. h) Images of three exemplary bonded configurations, and corresponding tensile force-displacement curves compared to model.

474
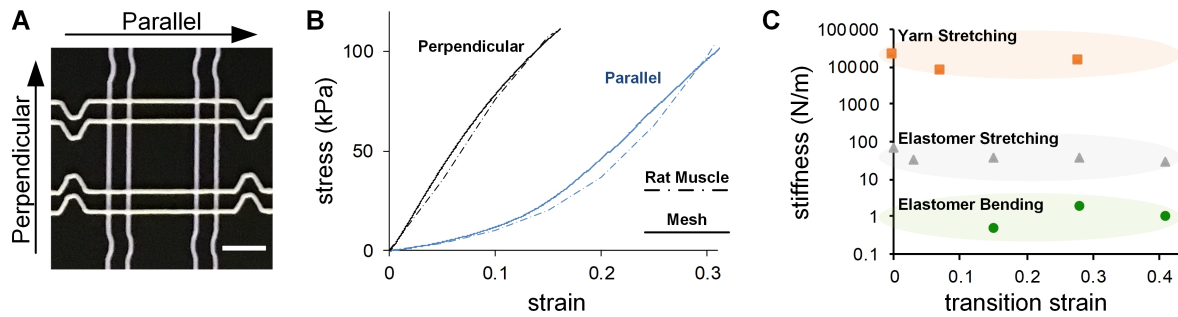
Figure 3: Tailoring mesh mechanics to match tissue. a) image (scale bar 4mm) and b) stress

strain data of a mesh unit cell (solid line) whose tensile response in two directions emulates that

of muscle tissue as measured by Takaza et al.[21] (dashed line). c) Range of stiffness and transition

strains achieved by varying material composition and geometry in the mesh. The stiffness is

measured as the approximately linear region before or after the transition from bending to

stretching. Yarn stretching refers to incorporation of synthetic fiber, as in Fig. 5.

481
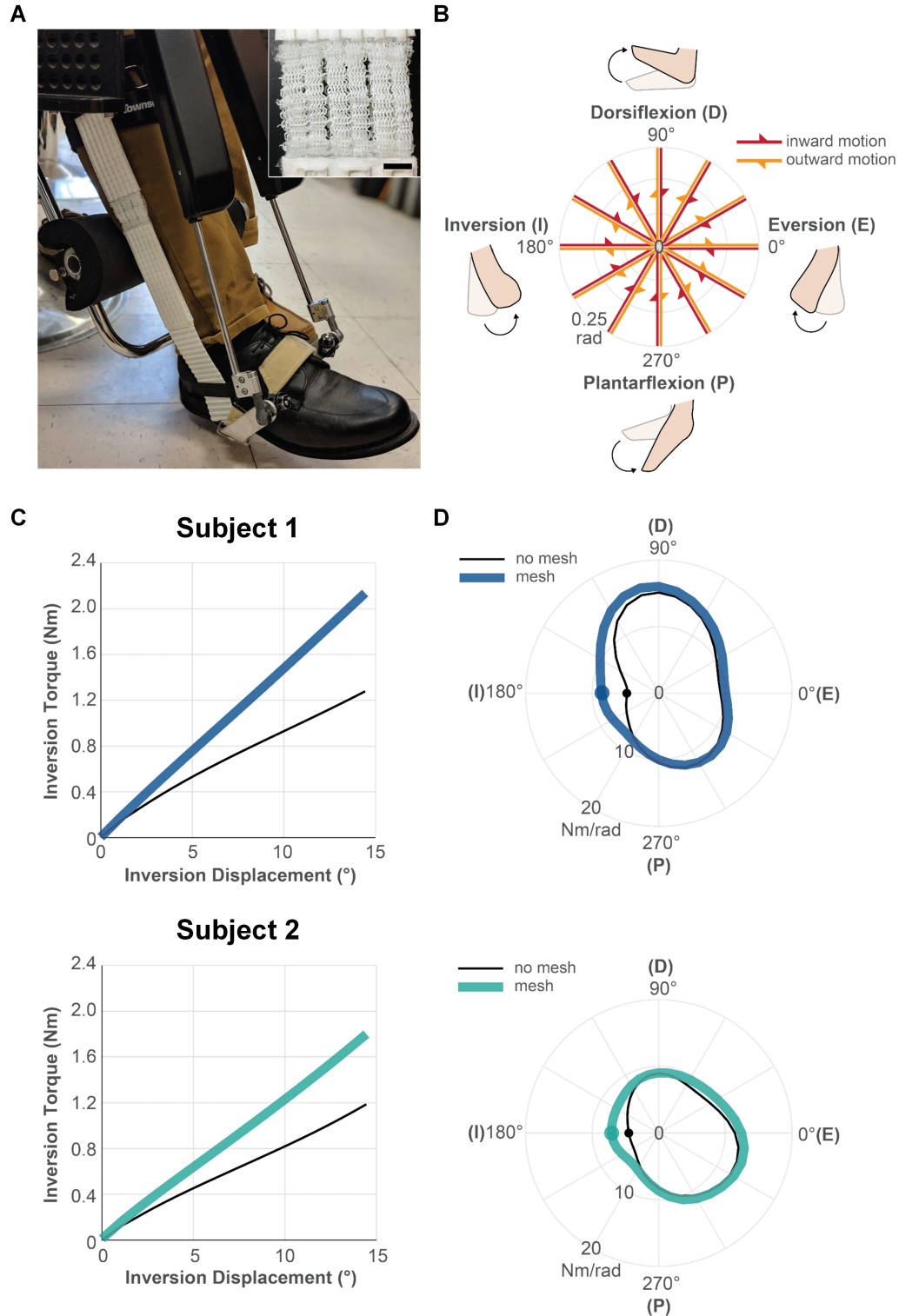
Figure 4: Demonstration of digitally tailored mesh for resisting ankle inversion. a) A non-linear mesh incorporated into an ankle brace and the attachment of this brace to the robot used for ankle stiffness measurement. Inset shows the mesh portion of the brace (scale bar 10mm) b) Schematic

486   showing the 12 directions the ankle is rotated in in order to generate the stiffness measurements.

487   c) Plots of the torque vs angular displacement in inversion for two human subjects. d) Stiffness

488   distribution in the ankle of these two subjects, with and without the mesh device.

489
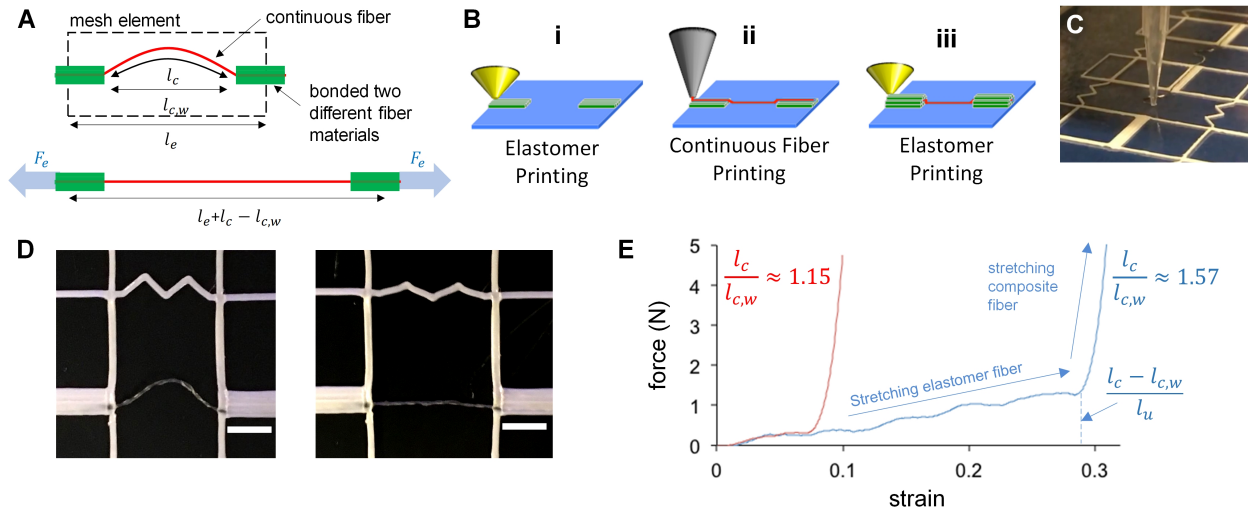
Figure 5: Reinforcing digitally tailored mesh using continuous fiber a) Schematic showing how a stainless steel thread is placed within the bonded elastomer mesh, with a free length of slack. b) Method of patterning continuous fiber mechanism including sandwiching between extruded layers. c) Image of fiber printing. d) Image of unit cell with continuous fiber (scale bar 4mm), unstretched (left) and stretched (right). e) Force-strain curves for two exemplary fiber-reinforced mesh samples, with different initial slack, where l_u denotes the unit cell length (smoothed with Savitzky-Golay filter).

499
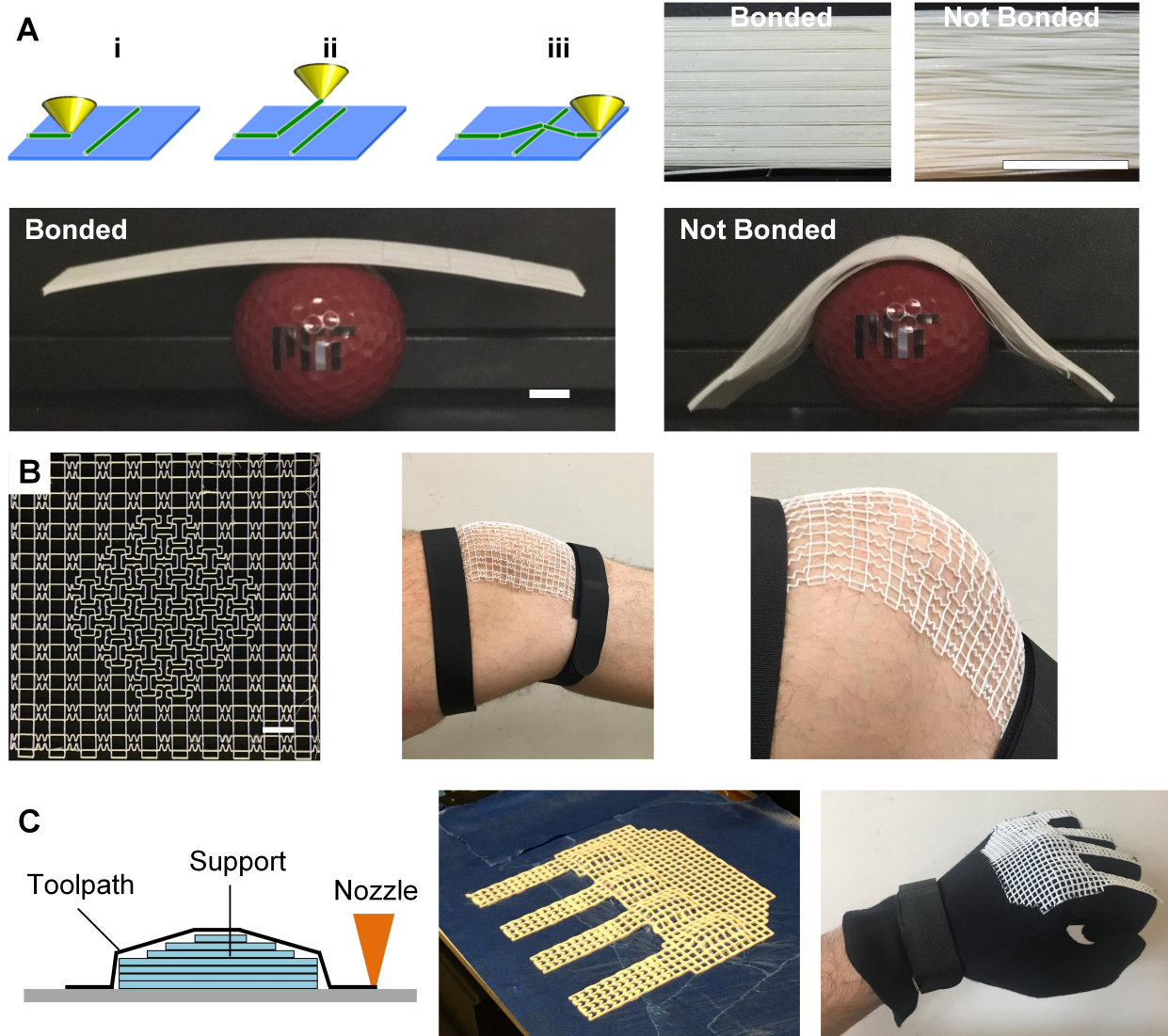
Figure 6: Additional capabilities of mesh printing. a) Modulation of fiber-fiber bonding using 3D

toolpaths that allow the fiber to cool before it touches the previous, orthogonally-placed fiber.

This results in the non-bonded swatch having noticeably greater drape (scale bar 10mm). b) A

mesh (scale bar 10mm) with locally patterned negative Poisson's ratio unit cells, which featuring

anisotropic mechanics and showing it's ability to conform to a knee. c) Printing of conformal

mesh onto a template, and after which the mesh is sewn onto a glove. This mesh-enhanced glove

exerts a restoring force on the fingers when the fist is clenched, as is commonly necessary in

stroke rehabilitation.

508 Explicit toolpath programming in an additive manufacturing process can enable flexible mesh
509 materials with digitally tailored mechanical properties and geometry. The work demonstrates that
510 tensile mesh mechanics can be engineered to match the nonlinear response of muscle, produce an
511 ankle brace with directionally specific inversion stiffness, and presents further concepts for
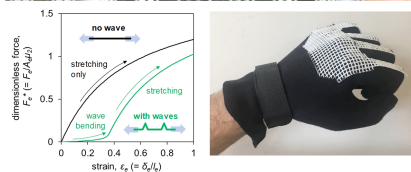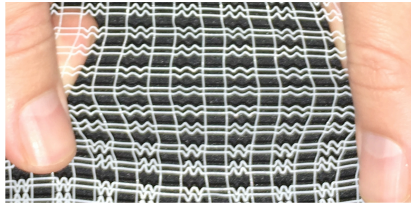512 tailoring their 3D geometry for medical applications.
513
514 **Keyword** Additive Manufacturing
515

516 Sebastian W. Pattinson,[*] Meghan E. Huber, Sanha Kim, Jongwoo Lee, Sarah Grunsfeld, Ricardo

517 Roberts, Gregory Dreifus, Christoph Meier, Lei Liu, Neville Hogan, A. John Hart*

518
519 **Additive Manufacturing of Biomechanically Tailored Meshes for Compliant Wearable and**

520 **Implantable Devices**

521

522 **Supporting Information**

523 **Additive Manufacturing of Biomechanically Tailored Meshes for Compliant Wearable and**

524 **Implantable Devices**

525

526 *Sebastian W. Pattinson,* *Meghan E. Huber, Sanha Kim, Jongwoo Lee, Sarah Grunsfeld, Ricardo*

527 *Roberts, Gregory Dreifus, Christoph Meier, Lei Liu, Neville Hogan, A. John Hart**

528

529

530 **An analytical/numerical model for extension behavior of single element with two waves**

531 *Extension by fiber stretching.*

532 For a Mooney-Rivlin material, the engineering stress σ_e under uniaxial extension applied to a

533 single element is expressed as[1]

$$\sigma_e = \left(\mu_1 + \frac{\mu_2}{\lambda_{e,s}}\right)\left(\lambda_{e,s} - \frac{1}{\lambda_{e,s}^2}\right) \quad \text{(Equation S1)}$$

534

535 where μ_1 and μ_2 are material constants and $\lambda_{e,s}$ is the element extension by the fiber stretching.

536 Accordingly, the applied force F_e can be given as

$$\frac{F_e}{A_e C_1} = \left(1 + \frac{\mu_2}{\mu_1}\frac{1}{\lambda_{e,s}}\right)\left(\lambda_{e,s} - \frac{1}{\lambda_{e,s}^2}\right) \quad \text{(Equation S2)}$$

537

538 where A_e and l_e is the original cross-sectional area and original length of the element respectively.

539 And the extension displacement by stretching can be given as

$$\delta_{e,s} = l_e\left(\lambda_{e,s} - 1\right) \quad \text{(Equation S3)}$$

540

541

542 *Extension by fiber bending.*

543   When an element having a wave with height h_w and width l_w is under extension by a tensile force

544   F_e, the fibers at the edges in the wave will bend until the equilibrium angle θ. Assuming the

545   bending stiffness at the edge is constant and given as K', a small amount of bending by increase

546   in tensile force can be expressed as

547
$$dM_e \cong dF_e \left\{ h_w^2 + \left(\frac{l_w}{2} \right)^2 \right\}^{1/2} \sin\theta \cong -K'd\theta \qquad \text{(Equation S4)}$$

548   where M_e is the moment at the edge, and θ is the angle of the bended fiber edge. Accordingly, the

549   required force to bend the wave to an angle of θ is given as

550

551
$$\int_0^{F_e} dF_e = -K' \left\{ h_w^2 + \left(\frac{l_w}{2} \right)^2 \right\}^{-1/2} \int_{\theta_0}^{\theta} \csc\theta \, d\theta \qquad \text{(Equation S5)}$$

552
$$F_e = K' \left\{ h_w^2 + \left(\frac{l_w}{2} \right)^2 \right\}^{-1/2} [\log\{\cot\theta + \csc\theta\} - \log\{\cot\theta_0 + \csc\theta_0\}] \text{ (Equation}$$

553
$$\text{S6)}$$

554   where θ_0 is the original angle of the wave edge as

555
$$\tan\theta_0 = \frac{2h_w}{l_w} \qquad \text{(Equation S7)}$$

556   Finally, the extension displacement by bending of a fiber element having two waves can be

557   expressed as a function of the equilibrium angle θ as

558
$$\delta_{e,b} = 4 \times \left\{ h_w^2 + \left(\frac{l_w}{2} \right)^2 \right\}^{1/2} [\cos\theta - \cos\theta_0] \qquad \text{(Equation S8)}$$

559

560   By numerical calculation using Eqs. [S2], [S6], [S8], we can acquire force-strain and stiffness-

561   strain curves for a known values of material constant μ_1 and μ_2, bending stiffness K', element

562   length l_e, element cross-sectional area A_e, wave width l_w. Table S1 shows the values used for the
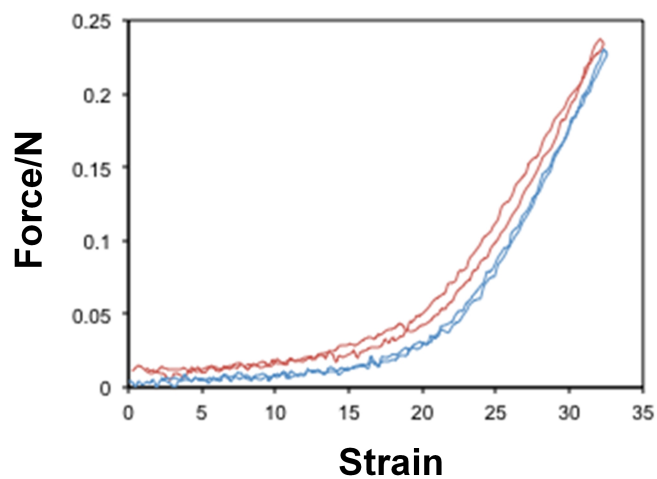
563   plots in Fig. 2a.

564

565   Table S1. Input values for the model estimation.

Input Variables	μ_1	μ_2	K'	l_e	A_e	l_w
Units	MPa	MPa	N·mm	mm	mm^2	mm
Values	0.1	0.54	0.1	24	0.79	2.5

566

567

568

Figure S1: Fatigue behavior of an individual fiber stretched to 32% strain once (red) and 1835

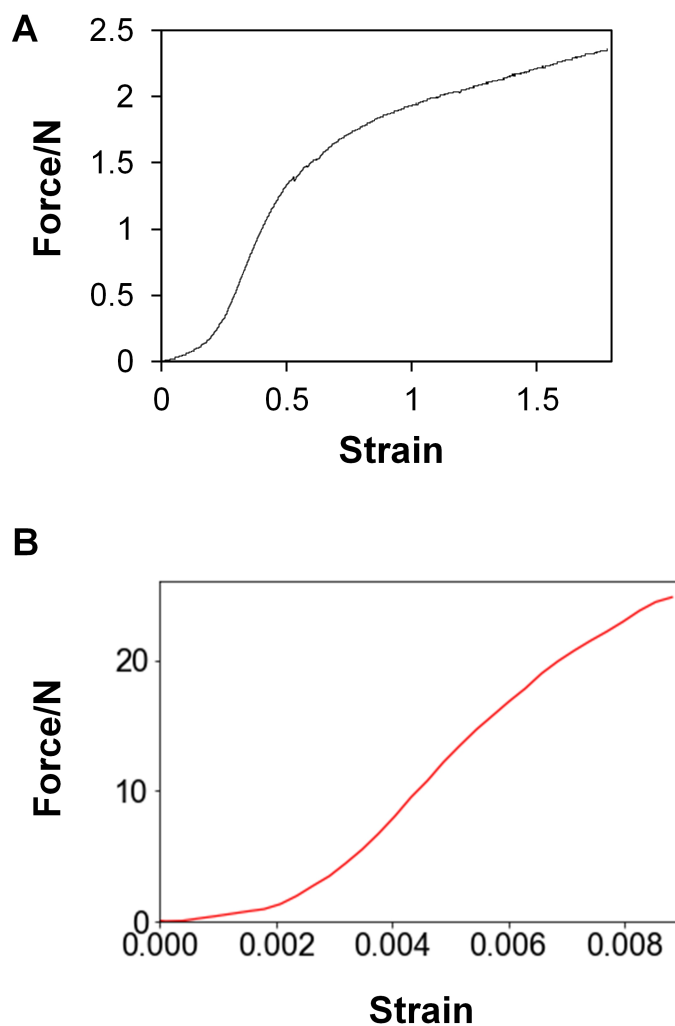570   times (blue).

571

572

573

574

575

576 **Figure S2:** a) All-elastomer unit cell mesh tensile test to failure. b) Unit cell with straight

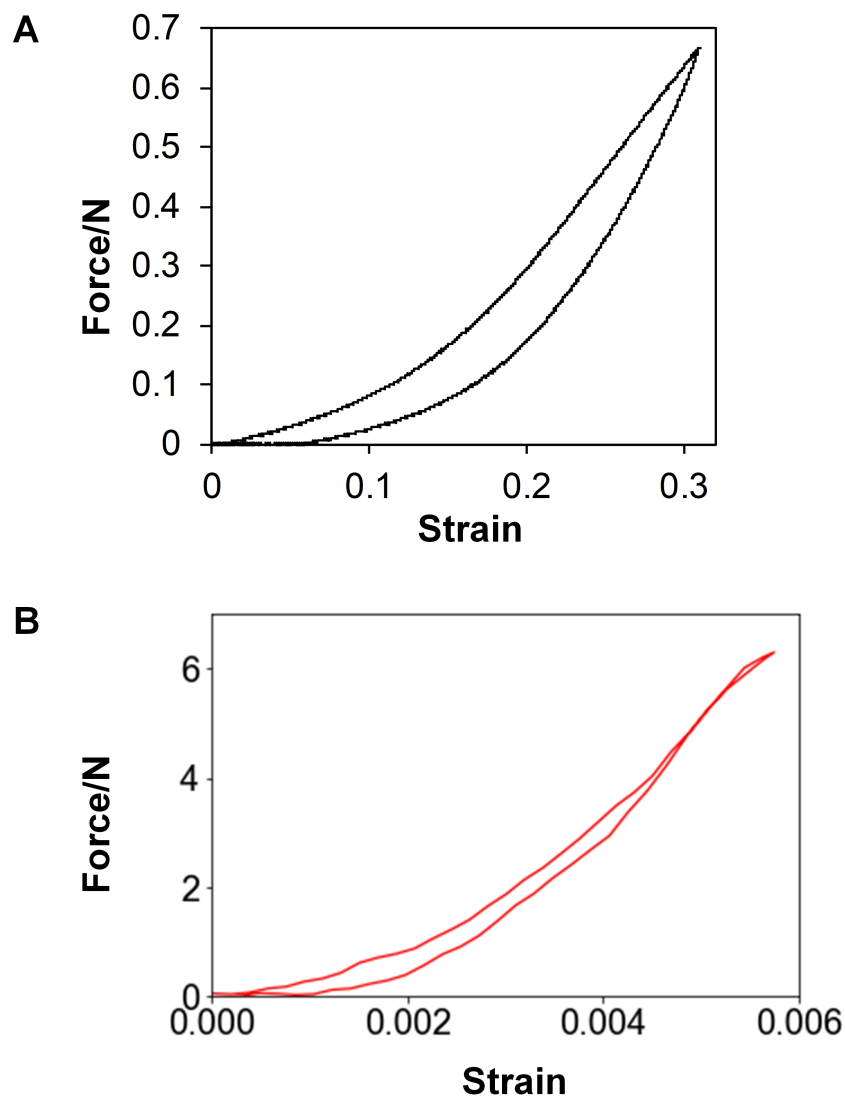577 continuous fiber tensile test to failure (smoothed with Savitzky-Golay filter).

578

579

580

581 **Figure S3:** a) All-elastomer unit cell mesh single load-unload cycle. b) Unit cell with straight

582 continuous fiber single load-unload cycle (smoothed with Savitzky-Golay filter).

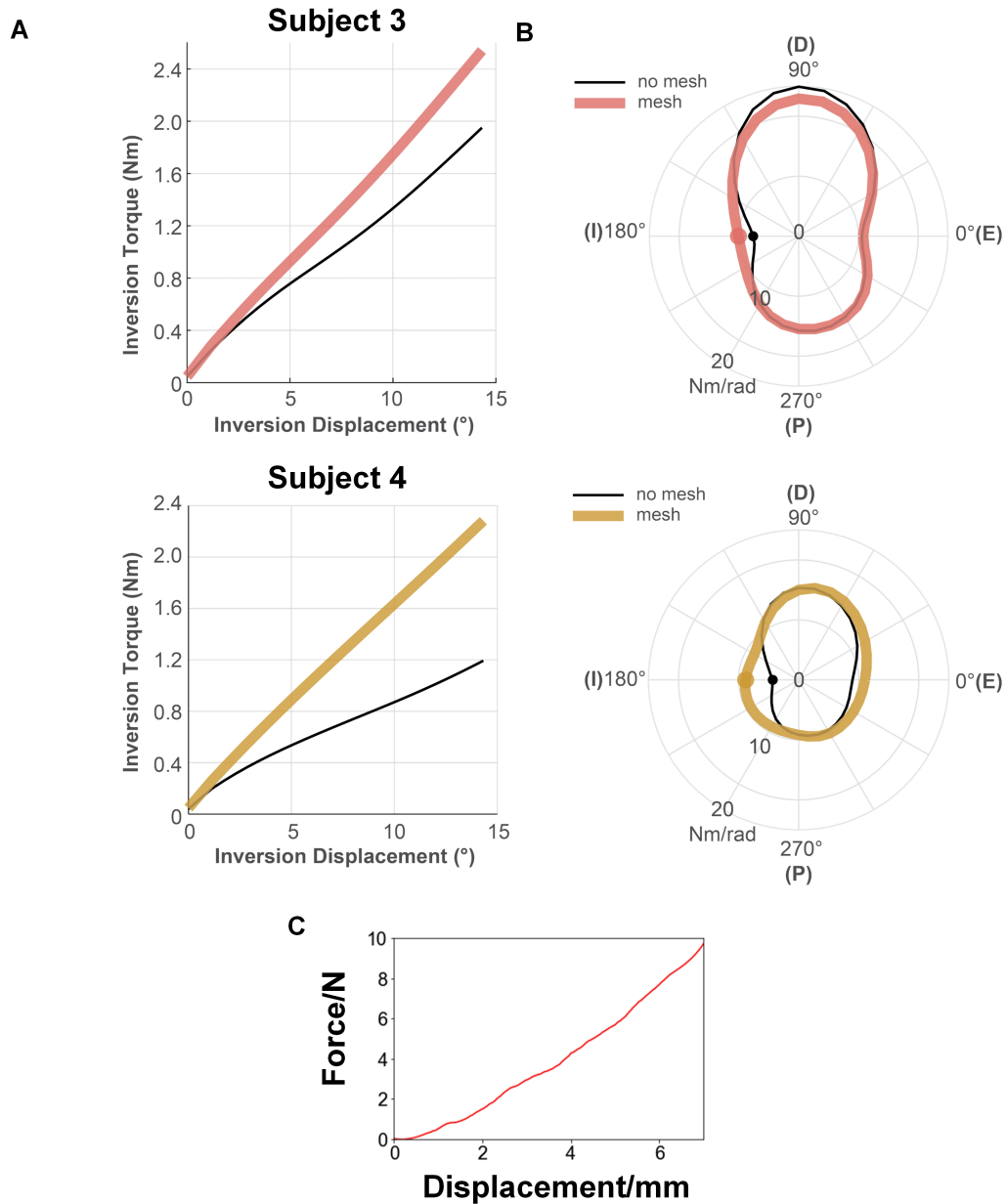583

584

A

Subject 3

Subject 4

B

C

Figure S4: a) Plots of the torque vs angular displacement in inversion for further two human subjects. b) Stiffness distribution in the ankle of these two subjects. c) Force vs. displacement curve for the ankle brace (smoothed with Savitzky-Golay filter).

590 **Supporting Reference**

591   [1]   A. Bower, Applied Mechanics of Solids; CRC Press, 2009